Supporting Information: Navigation of brain networks

Caio Seguin, Martijn P. van den Heuvel, Andrew Zalesky

Overview

This supporting document provides details on the acquisition and preprocessing of the analyzed connectivity data. We also provide descriptions of the network measures and methods applied throughout this work. Finally, we include supplementary and replication analyses that indicate the robustness and universality of the results reported in the main manuscript. Figure numbering is with respect to the ordering of references in the main manuscript.

Materials and Methods

Connectivity data

Mouse. The Allen Institute for Brain Science mapped the mesoscale topology of the mouse nervous system by means of anterograde axonal injections of a viral tracer [1]. Using two-photon tomography, they identified axonal projections from the 469 injections sites to 295 target regions. Building on these efforts, Rubinov and colleagues constructed a bilaterally symmetric whole-brain network for the mouse, comprising $N = 112$ cortical and subcortical regions with 53% connection density [2]. Connections represent interregional axonal projections and their weights were determined as the proportion of tracer density found in target and injected regions. Connection weights followed a log-normal distribution and graph-theoretical analyses of the constructed topology revealed many organisational similarities to the human connectome.

Macaque. Markov and colleagues applied 1615 retrograde tracer injections to 29 of the 91 areas of the macaque cerebral cortex, spanning occipital, temporal, parietal, frontal, prefrontal and limbic regions [3, 4]. This resulted in a 29×29 directed interregional subnetwork of the macaque coritco-cortical connections. Connection weights were estimated based on the number of neurons labelled by the tracer found in source and target regions, relative to the amount found in whole brain. In line with other tract-tracing studies, the network showed high connection density (66%) and weights were distributed log-normally.

Human data acquisition and preprocessing. Minimally preprocessed diffusion weighted MRI data from 75 unrelated healthy participants (age 22–35, 40 females) was obtained from the Human Connectome Project (HCP) [1] [5]. Spin-echo planar diffusion weighted imaging was performed in a customized Siemens Skyra 3T scanner according to the following parameters: 5520 ms repetition time, 89.5 ms echo time, 78 degree flip angle, 160 degree refocusing flip angle, 210×180 mm filed of view, 168×144 matrix, 1.25 mm isotropic voxels, 3 shells of b=1000, 2000 and 3000 s/mm2 and approximately 90 diffusion weighted directions per

[1] HCP participants ID: 100206, 100307, 100408, 101006, 101107, 101309, 101915, 102109, 102513, 102614, 102715, 102816, 103111, 103212, 103414, 103515, 103818, 104012, 105014, 105115, 105216, 105620, 106016, 106319, 106521, 106824, 107018, 107321, 107422, 107725, 108020, 108121, 108222, 108323, 108525, 108828, 109123, 109830, 110007, 110411, 110613, 111009, 111211, 111312, 111413, 111716, 112112, 112314, 112516, 112920, 113215, 113316, 113619, 113922, 114217, 100610, 102311, 104416, 118225, 105923, 111514, 114823, 115017, 125525, 128935, 131722, 140117, 146129, 146432, 155938, 156334, 157336, 158035, 158136, 162935.

www.pnas.org/cgi/doi/10.1073/pnas.1801351115

gradient table. The obtained diffusion images were submitted to the HCP diffusion preprocessing pipeline [6] consisting of: 1) b_0 intensity normalization, 2) top-up EPI distortion correction, 3) Eddy current distortions and subject motion correction, 4) gradient distortion correction and 5) resampling to 1.25mm native structural space. Refer to [6, 7] for further details on HCP diffusion MRI acquisition and preprocessing.

Minimally preprocessed resting-state functional MRI data from the same 75 participants was also obtained from the HCP. Data acquisition consisted of four 14m33s runs, two runs (right-to-left and left-to-right phase encodings) in one session and two in another session, with eyes open with relaxed fixation on a projected bright cross-hair on a dark background (and presented in a darkened room). Data collection was performed in a customized Siemens Skyra 3T scanner according to the following parameters: gradient-echo EPI sequence, 720 ms TR, 33.1 ms TE, 52 degree flip angle, 208 × 180 mm FOV, 104 × 90 matrix, 2.0 mm slice thickness, 72 slices, 2.0 mm isotropic voxels, 8 multiband factor and 0.58 ms echo spacing. Acquired images were preprocessing according to the HCP functional preprocessing pipeline [6], which involves: 1) spatial and gradient distortion corrections, 2) correction of head movement, 3) intensity normalization 4) single spline re-sampling of EPI frames into 2mm isotropic MNI space and 5) HCP's FIX+ICA pipeline for the removal of temporal artefacts. Refer to [6, 8] for further details on HCP resting-state functional MRI acquisition and preprocessing.

Human cortical parcellation. Connectome analyses are sensitive to the number of nodes used to reconstruct brain networks [9]. In order to assess the validity of our results across connectomes defined over different granularities of cortical segmentations, we generated parcellations of the human cerebral cortex containing $N = 256, 512, 1024$ regions. In addition, we also mapped connectomes using the Glasser Atlas [10], a multi-modal cortical parcellation built from the combination of structural, diffusion and functional imaging data from HCP participants.

We developed an algorithm to generate high-resolution cortical parcellations by means of sub-dividing an input low-resolution parcellation. Starting from a well established anatomical atlas ($N = 68$) [11] defined on FreeSurfer's (`https://surfer.nmr.mgh.harvard.edu/`) *fsaverage* cortical sheet, each surface region was subdivided according to three criteria: (i) the resulting number of regions is specified by the user as a power of 2; (ii) subdivisions must respect the original anatomical boundaries, so that all resulting parcels can be attributed to a single anatomical structure; and (iii) each resulting sub-region has approximately the same surface area. Criterion (i) allows for a systematic investigation of the robustness of graph theory measures to variations in parcellation resolution. Criterion (ii) ensures that the resulting parcellation comprises biologically meaningful regions that can be assigned to a single anatomical input region. Finally, criterion (iii) minimizes tractography biases related to the surface area and volume of regions. Importantly, defining the parcellations over the cortical surface ensures that every grey matter region has an interface with white matter, making it accessible to tractography streamlines.

Input low-resolution regions were divided based on their size (number of vertices in the cortical sheet mesh) and the desired number of high-resolution output regions. Large input regions originated many output regions, while small input regions gave rise to few output regions. K-means++ [12] applied to the spatial coordinates of vertices was used to perform region division, leading to evenly sized, spatially contiguous, tile-shaped output regions (Fig. S16). The resulting cortical surface parcellations were registered to native

subject space and projected into parcellation volumes using Connectome Workbench (`https://www.humanconnectome.org/software/connectome-workbench`, [13]).

While cortical regions are commonly defined in terms of a surface mesh, representations of subcortical structures remain voxel-based [6]. Parcellating subcortical regions is therefore more challenging and requires different methodologies to those that we have applied to the cortex. For this reason, subcortical regions were not included in the connectomes reconstructed in this study.

Human network mapping. Structural networks (connectomes) were mapped for each individual using a deterministic tractography [14] pipeline from the MRtrix3 software (`http://www.mrtrix.org/`, [15]). Diffusion tensors were estimated from the preprocessed diffusion weighted images using a iteratively reweighted linear least squares estimator. White matter masks was extracted from structural segmentation files provided by the HCP. White matter boundaries were dilated by 1 voxel to fill potential gaps between grey and white matter caused by slight imperfections in subject registration. Streamlines were uniformly seeded from the white matter mask and tracked along diffusion tensor directions (eigenvectors) until they exited the mask into grey matter or reached a voxel with low fractional anisotropy (FA) (FACT tracking algorithm, 5×10^6 streamlines, 0.5 mm tracking step-size, 400 mm maximum streamline length and 0.1 FA cutoff for termination of tracks). Connection strength between any pair of regions was determined as the number of streamlines with extremities located in the regions, resulting in $N \times N$ weighted connectivity matrices. In order to capture general patterns of brain organization and filter out idiosyncratic variation, a group average connectome was computed by averaging the individual connectomes of all 75 participants. Subsequent network analyses were carried out on the group-averaged connectome.

Functional networks were mapped using command line tools from Connectome Workbench. For each subject, four runs of preprocessed resting-state fMRI volumes were averaged together and projected onto the subject's cortical surface. The functional activation profile of each region was described as a single time series by averaging the signal of all the vertices comprised in the region. Pairwise functional connectivity was computed by means of the Pearson correlation coefficient between regional time series, resulting in $N \times N$ weighted connectivity matrices. A group-averaged functional network comprising the 75 individual connectivity matrices was computed and used in subsequent analyses.

Network analysis

Connection weights and lengths A weighted connectome can be expressed as a matrix $W \in \mathbb{R}^{N\times N}$, where W_{ij} is the connection weight between nodes i and j. Connection weights are a measure of similarity or affinity, denoting the strength of the relationship between two nodes (e.g., streamline counts in tractography or fraction of labelled neurons in tract tracing). Typically, the matrix of connection lengths L is computed from W by means of a weight-to-length transformation that monotonically remaps strong weights into short lengths and weak weights into long lengths. This way, connection lengths denote the dissimilarity, distance or travel cost between nodes. Defining nodal relationships in terms of lengths allows for the computation of short communication paths.

Connection length matrices were computed as follows. In the binary case, $L^{bin} \in [0, 1]$ denoting only the presence or absence of a connection in W. In the weighted case, $L^{wei} = -\log_{10}(W/max(W))$ ensuring a monotonic weight-to-length transformation that produces

log-normally distributed connection lengths and attenuates extreme connection weights [16, 17] (for human connectomes weighted by streamline counts, $L^{wei} = -\log_{10}(W/max(W)+1)$ to avoid remapping the largest weight to a length of zero.) In the distance-based case, connections lengths denote the physical distance between directly connected nodes, with $L^{dis} = D \odot L^{bin}$, where D is the Euclidean distance matrix between node pairs. Hence, shortest paths computed on L^{bin}, L^{wei} and L^{dis} minimize the number of traversed connections (hops), maximize the strength and reliability of traversed connections and minimize the physical distance traversed between nodes, respectively.

Connectome thresholding. Density-based thresholding of connection weights was applied to the group-averaged connectome in order to filter out potentially noisy and spurious connections [18]. A density threshold of 15% consists of keeping the top 15% highest weighted connections and deleting the remaining ones. Since the true connection density of the brain remains unknown [19], we sought to replicate our key analyses for a range of 5% to 60% connection density thresholds, at 5% intervals.

Null network models. Six null network models were used in this work: (M1) topologically randomized (rewired) networks, (M2) spatially randomized (repositioned) networks, (M3) topologically randomized cost-preserving networks, (M4) progressively randomized networks, (M5) progressively clusterized networks and (M6) progressively randomized, navigability-improving networks.

Null models (M1), (M2) and (M3) were employed in the sections *Navigability of the human connectome* and *Navigability of non-human mammalian connectomes*, while (M4), (M5) and (M6) were used in section *Connectome topology and navigation performance*.

Topological randomized networks (M1) were computed by rewiring the connectome using the Brain Connectivity Toolbox (`https://sites.google.com/site/bctnet/`, [20]) implementation of the Maslov-Sneppen algorithm [21]. Rewiring was carried out by swapping each connection once (on average) while preserving the network original degree distribution and connectedness. Spatially randomized networks (M2) had the spatial coordinates or their nodes randomly swapped with each other, while maintaining the topology unaltered.

For reasons of computational tractability, navigation performance in the human connectome (*Navigability of the human connectome*) was benchmarked against ensembles of 1000 ($N = 256$), 1000 ($N = 360$), 500 ($N = 512$) and 100 ($N = 1024$) topologically randomized networks (M1), per connection density threshold. Ensembles of the same size were generated for spatially randomized networks (M2). The benchmarking of non-human connectomes (*Navigability of non-human mammalian connectomes*) was done by constructing ensembles of 10^4 topologically randomized networks (M1) and 10^4 spatially randomized networks (M2). Non-parametric P-values for S_R, E_R^{bin}, E_R^{wei} and E_R^{dis} were computed as the proportion of times null networks outperformed the empirical connectomes. Cost-preserving randomized networks (M3) showed markedly improved navigability when compared to models (M1) and (M2). Therefore, to ensure an accurate characterization of the statistical differences between the navigability of cost-preserving null networks and empirical connectomes, we generated larger ensembles of 10^4 ($N = 256$), 10^4 ($N = 360$), 10^4 ($N = 512$) and 500 ($N = 1024$) cost-preserving networks for the human connectomes; and 5000 cost-preserving networks per non-human species (see *Cost-preserving topological randomization* for further details).

Progressively randomized networks (M4) were obtained by the same rewiring process as topologically randomized networks (M1), consisting simply of partially rewired networks for

which only a fraction of connections have been swapped. Progressively clusterized networks (M5) were produced by an adaptation of the (M4) procedure that only considers connection swaps that lead to an increase in the overall clustering coefficient of the network. The randomizing–clusterizing routine (*Connectome topology and navigation performance*) was repeated 100 times for $N = 256, 360, 512$, with E_R^{bin} and E_R^{wei} re-computed once every 5 connection swaps. The construction of progressively randomized, navigability-improving networks (M6) is detailed at *Optimizing connectome navigability with topological rewiring.*

Navigation centrality. The node navigation centrality of node i defined as $c(i) = \sum_{s \neq i \neq t} \pi_{st}(i)$, where $\pi_{st} = 1$ if the successful navigation path from s to t passes through i and $\pi_{st} = 0$ otherwise. In order to define a measure of edge navigation centrality (ENC), we first defined $c(i,j) = \sum_{s \neq t; i \neq j} \pi_{st}(i,j)$, where $\pi_{st}(i,j) = 1$ if the successful navigation path from s to t traverses the connection from node i to node j, and $\pi_{st}(i,j) = 0$ otherwise. Due to the asymmetric character of navigation, $c(i,j) \neq c(j,i)$. For simplicity, we adopted a symmetric definition of edge navigation centrality given by $c_{sym}(i,j) = (c(i,j) + c(j,i))/2$.

Node (edge) betweenness centralities were computed using the Brain Connectivity Toolbox (`https://sites.google.com/site/bctnet/`, [20]), representing the absolute number of shortest paths that pass through each node (edge) of the network.

Navigation and functional connectivity. Our implementation of navigation identifies paths based on the Euclidean distance between network nodes. Thus, a natural definition of navigation path length is to consider the physical distance traversed from one node to another. For our FC analysis, we defined navigation path length from i to j as $\Lambda_{ij}^{nav} = log_{10}(D_{iu} + ... + D_{vj})$, where $\{u, ..., v\}$ is the sequence of nodes visited during navigation from i to j and D is the Euclidean distance matrix between node pairs.

The logarithmic transformation leads to a better differentiation of the distance covered by short navigation paths (Fig. S17), leading to an expansion of the left tail (short navigation distances) of the navigation path length distribution and a compression of the right tail (long navigation distances). The transformation leads to stronger correlations with FC, suggesting that a nuanced characterization of short communication paths might play an important role in understanding the relationship between structural and functional brain networks.

Supplementary analyses

Navigability of individual human connectomes. In order to confirm the results obtained for the group-averaged human connectome, we evaluated the navigability of each individual's connectome separately for several connection densities and parcellation resolutions. The navigability of individual connectomes was consistent with group-averaged performance ($S_R = 95\%$, $E_R^{bin} = 84\%$, $E_R^{wei} = 63\%$ and $E_R^{dis} = 83\%$, averaged over all individuals, for $N = 360$ at 15% connection density).

We tested the null hypothesis of equality in navigation performance between males and females, as well as between three age brackets. Our sample consisted of 35 males and 40 females; and 11, 33 and 31 individuals aged between 22 to 25, 26 to 30 and 31 to 35 years, respectively. Statistical testing was performed on the area under the curve (AUC) of the navigation performance measures shown in Figures S8 and S7. In particular, a three-way analysis of variance (F-test) was used to test the null hypothesis of equality in the AUC between the three age brackets, while a two-sample t-test was used to test for differences in

the AUC between males and females. We found significant differences in the navigability of age groups across all parcellation resolutions (Table S1), with navigation performance decreasing with age. This result is in line with previous analyses suggesting a decrease in measures of network efficiency with age [22]. No significant difference in navigation performance between genders was found. Individual connectomes mapped for representative males and females from each of the three age brackets ($N = 360$, 15% connection density) were significantly more navigable than rewired, repositioned and cost-preserving rewired null networks (Fig. S6).

Navigation with scaling of streamline counts. A common practice in connectomics studies based on white matter tractography is to scale streamline counts by average fiber lengths [23]. This is motivated by the notion that certain tractography algorithms are biased towards overestimating the streamline count of long fiber bundles, although it is important to remark that this effect varies substantially between algorithms and streamline seed strategies, with grey-matter seeding strategies often *underestimating* the streamline count of long fibers [24]. We chose not to perform distance-based scaling, since this would impart information about the distance between nodes in each connection weight, potentially leading to an artificial improvement in navigation performance. However, it is then possible that the observed values of E_R^{wei} are a result of the uncorrected tractography bias towards long fiber bundles, since long range connections would be more efficient for both streamline count and distance-based path length regimes. In order to test for this issue, we recomputed navigation performance after dividing streamline counts by the Euclidean distance between nodes. As initially hypothesized, this transformation led to slight improvements in navigation performance across parcellation resolutions and connection density thresholds (orange curve, Fig. S5).

Similarly, streamline count are often normalized by the volume of brain regions [23]. This is motivated by the notion that the number of streamlines terminating in a certain region is influenced by the volume (or surface area) of that region, leading to an artificial increase (decrease) in the strength of network nodes corresponding to large (small) cortical regions. In order to address this potential issue, we computed the navigability of the human connectome constructed after normalizing connection weights W_{ij} by $W_{ij} = (NOS_{ij})/(V_iV_j)$, where NOS_{ij} is number of streamlines between regions i and j and V_i is the volume of region i. This transformation lead to visible improvements in navigation performance, especially for E_R^{wei}, across several connection density thresholds and parcellation resolutions (yellow curve, Fig. S5).

Alternative distance measures for navigation. Navigation was performed using the Euclidean distance between region centroids as the distance measure between network nodes. While this approach has been extensively used as an approximation of the distance between neuronal populations [25, 26, 27], it has potential shortcomings.

First, brain regions such as the motor, pre- and post-central cortices are long and narrow, rendering a centroid-based distance measure not representative of distances between voxels. In order to address this potential issue, we defined the distance between nodes as $D_{max}(i,j) = max(d_{\alpha\beta})$ and $D_{min}(i,j) = min(d_{\alpha\beta})$, where $d_{\alpha\beta}$ is the set of pairwise Euclidean distances between all voxels comprising regions i and j, $\alpha \in i$ and $\beta \in i$. The purple and green curves in Fig. S5 show the navigation performance obtained for D_{max} and D_{min}, respectively, for several connection densities and parcellation resolutions. The ob-

tained results are consistent with previously presented analyses (Fig. S5, blue curve), with the marked exception of E_R^{dis} when navigation is computed over D_{min}. This discrepancy is caused by the skewed distribution of connection lengths for D_{min} (Fig. S18A). For any pair of adjacent regions i, j, $D_{min}(i, j) \propto 1$. Distance-based shortest paths are heavily mediated by these short connection lengths, which leads to unrealistic shortest paths composed of many hops but very small path lengths (Fig. S18B-D). For this reason, D_{min} is most likely an unsuitable distance measure for shortest paths.

Second, we assessed the navigability of the human connectome when introducing increasing amounts of noise to centroid coordinates. We added noise sampled from a Gaussian $(0, \sigma)$ to the spatial coordinates of each region centroid. We assessed the navigability of the human connectome (group-averaged, $N = 360$ at 15% connection density) using an Euclidean distance matrix computed on the noisy coordinates, for increasing values of σ (Fig. S4). We found that all measures of navigation performance (averaged over 100 simulations) were robust to small amounts of noise and gradually deteriorated as the centroid coordinates became noisier. Robustness to small amounts of noise is important when considering potential errors in node spatial coordinates due to, for instance, slight imperfections in image registration; whereas marked navigability reductions for large amounts of noise serves as an alternative null model that reiterates the important of the spatial embedding of brain networks.

Finally, quantifying inter-regional distances with measures other than the Euclidean distance between regional centroids (e.g. fiber-tract length or tract myelination) may provide more realistic distance estimates and thereby improve connectome navigability. Fiber-tract length may represent a more realistic measure of the distance travelled between two nodes. However, in addition to the distance between structurally connected nodes, navigation also depends on the distance between structurally unconnected nodes, for which fiber-tract lengths cannot be computed. Techniques of fiber interpolation [27] or heavily seeded probabilistic tractograms leading to near-complete connectivity matrices [28] could guide future work on navigation based on fiber lengths.

Cost-preserving topological randomization. Longer connections are typically assumed to demand greater metabolic resources, and thus connection length is often used as a proxy measure of metabolic cost [19, 29]. In this study, we defined network cost as the sum of the Euclidean distances between connected nodes [27, 30, 31].

We implemented a rewiring routine that generates null networks that preserve the original network's degree distribution and number of connected components, while approximately preserving its cost. The routine is an adaptation of the Maslov-Sneppen algorithm [21] that only considers connection swaps that do not alter the resulting network's cost by more than a user defined threshold (set to 1mm). We assessed how closely null networks matched original costs by means of a relative cost measure $cost_{rel} = cost_{null}/cost_{emp}$. Ideally, this ratio should be exactly 1, but because cost was matched up to a prescribed tolerance for each connection swap ($\pm$ 1mm), the a small difference in the cost of the empirical and null networks can accumulate with a growing number of swaps. Fixing the tolerance at 0 is not practical, since the vast majority of candidate swaps cannot lead to an exact preservation of cost. As shown in the results below, this strategy was able to match the total cost of connectomes within a 0.1% error margin.

Starting from the human connectome ($N = 360$), we generated 1000 cost-preserving rewired networks for each of several connection density thresholds. In addition, we gener-

ated 10^4 cost-preserving networks for the human connectome at parcellation resolutions of $N = 256, 512, 1024$ and 15% connection density threshold. Preserving network cost greatly improved the navigability of the null networks, as seen by the reduced gap between navigation performance measures computed on rewired and empirical networks (Fig. S3A-D). Despite this improvement, the human connectome remained significantly more navigable than the cost-preserving surrogate networks ($P < 10^{-4}$), across all navigation performance measures, parcellation resolutions (Fig. S3E) and connection density thresholds (with the exception of 5% connection density). Significance was assessed using a non-parametric P-value computed as the proportion of times null networks outperformed empirical connectomes.

Next, we next generated 5000 cost-preserving rewired networks for the macaque ($N = 29$) and mouse ($N = 112$) connectomes. For both species, the null hypothesis of equality in navigation performance between the empirical and cost-preserving null networks could not be rejected for any connection density (Fig. S9). Thus, preservation of network cost is sufficient to account for the efficiency of navigation in the non-human connectomes. The considered macaque connectome comprises a single hemisphere [4], and thus lacks long-range inter-hemispherical connections, which could potentially explain the non-significant results obtained for this species. However, this is not the case for the investigated mouse connectome [2]. In following, we provide several explanations of the importance of network cost to navigation performance, particularly for the non-human connectomes.

Network cost, being defined in terms of connection lengths, has a direct relationship with the distance between network nodes. A number of studies have documented the important influence of the spatial positioning of nodes in brain network topology [25, 27, 28], indicating that preserving network cost not only leads to null networks with more realistic spatial embedding, but also topological organization that more closely resembles that of empirical connectomes. Thus, the cost-preserving null model results in networks that (i) are less topologically random than the ones produced by simple rewiring routines, (ii) respect the original distance relationships between connectome nodes and (iii) match the original degree distribution of the connectome. In non-human species, preserving these three traits was sufficient to fully account for the extent to which brain networks are navigable. In contrast, the human connectome remained significantly more navigable than cost-preserving null networks. The human cortex exhibits more gyrification than those of the macaque and mouse [32, 33], resulting in a more complex anatomical configuration of cortical folding, and, consequentially, a more intricate spatial embedding. We hypothesized that, in order to facilitate navigation given this higher spatial complexity, the topology and geometry of the human connectome may have additional organizational factors not present in the mouse and macaque brains, and not captured by the cost-preserving null model.

Ultimately, the findings from the cost-preserving null model analysis reiterate the importance of connectome geometry for efficient communication under navigation routing, indicating that the relative spatial positioning of network nodes explains, to a large extent, the navigation performance of brain networks.

Optimizing connectome navigability with topological rewiring. We sought to test whether human connectome navigability could be improved (optimized) by topological rewiring explicitly seeking to improve navigation performance. More specifically, we implemented an adaptation of the Maslov-Sneppen rewiring routine [21] that only accepts connection swaps resulting in an increase of a given measure of navigation performance. In addition, we aimed preserved the total cost of connectomes during the connection swap

routine, where network cost was defined as the sum of the Euclidean distance between structurally connected node pairs [27,29,34]. Thus, topological rewiring was constrained to connection swaps between randomly chosen node pairs that (i) preserved connection density and degree-distribution; (ii) improved a measure of navigation performance; and (iii) did not result in a cost offset larger than a predefined threshold (set to 1mm). Connection swaps that did not simultaneously meet all three conditions were rejected.

Optimization was performed with respect to several different navigation performance measures. In the previous randomize/clusterize analysis we focused on E_R^{bin} and E_R^{wei}, quantifying how efficient navigation paths are in relation to shortest paths. However, seeking to optimize ratio measures by progressive alterations in topology could theoretically result in networks that are not efficient for navigation nor optimal routing, but show high efficiency ratios. For instance, in a regular lattice, both navigation and shortest paths have low absolute efficiencies but $E_R^{bin} = 1$. Thus, another possibility is to optimize "raw" measures of navigation performance (e.g., E^{bin} or E^{wei}) that capture the absolute efficiency of navigation paths.

Progressively altering network topology to optimize navigation is a time-intensive task, requiring the computation of navigation for each connection swap attempt. In contrast to the randomize/clusterize routine, the navigability of the networks generated in this analysis monotonically increases by design. As a result, in order to assess the room for improvement in navigation, it is necessary to perform enough connection swaps to adequately converge to an asymptote in the measures of navigation performance of the generated networks. We found that in the order of 10^6 connection swap attempts lead to a reasonable characterization of the margin to increase navigability.

We applied this swap routine to the human connectome (group-averaged, $N = 256, 360, 512$ at 15% connection density) aiming to optimize, in turn, E_R^{bin}, E_R^{wei}, E^{bin} and E^{wei}. We found that when explicitly optimizing these navigation measures, the margin for improvement in navigability is larger inferred from the randomize/clusterize analysis (Fig. S11). On average, the generated networks showed a 13%–17% increase in E_R^{bin}, while E_R^{wei} had a 18%–20% margin of improvement. Similarly, the swap routine lead to a 17%–20% improvement in E^{bin} and E^{wei} was increased by around 5% for $N = 256, 360$ and 13% for $N = 512$. In all cases, the majority of observed improvement took place in the first 10^6 swap attempts (87.5%, 88.1%, 88.6% and 88.0% of the average total improvement in E_R^{bin}, E_R^{wei}, E^{bin} and E^{wei}, respectively, for $N = 360$). Therefore, increasing connectome navigability quickly became more difficult as a function of swap attempts, suggesting that the observed improvements converge to an asymptote.

Importantly, the 5%–22% margin for navigability improvement identified by our connection swap analyses is not definitive. We attempted to optimize network navigability by means of a greedy connection swap strategy that is not guaranteed to converge to global maxima of navigation performance. Performing a higher number of navigation optimization connection swaps, or employing more sophisticated methodologies to alter connectome topology, could potentially result in more pronounced improvements to navigation.

There are many possible explanations for the fact that connectome navigability can be marginally improved with explicit optimization. First, evolutionary pressures for the development of desirable characteristics other than efficient communication are likely to have been influential in shaping connectome architecture. For instance, network robustness is conjectured to confer the brain resilience against lesions in cortical regions and white matter projections [30,35,36]. Second, the need to accommodate higher-order geometric constraints not captured by our length-based definition of network cost, such as the volumetric profile

Parcellation resolution	S_R		E_R^{bin}		E_R^{wei}		E_R^{dis}	
	P-value	F-stat	P-value	F-stat	P-value	F-stat	P-value	F-stat
256	0.02	4.05	0.75×10^{-4}	10.86	0.17	1.81	0.1×10^{-4}	10.40
360	0.02	4.03	0.001	6.87	0.02	4.05	0.003	6.07
512	0.26	1.36	0.03	3.75	0.06	2.95	0.05	3.14
1024	0.10	2.37	0.02	3.89	0.01	4.46	0.03	3.61

Table S1: Influence of age on connectome navigability. The table shows the P-values and F-statistics for a three-way analysis of variance of the AUC between three age brackets, computed for different navigation performance measures. Age significantly influenced connectome navigability, with navigation performance decreasing with age.

of axonal projections of different shapes and diameters [28], might result in sub-optimal arrangements of white matter fiber bundles within the brain. Third, it is plausible that certain patterns of connectivity between cortical regions, although sub-optimal from a communication efficiency standpoint, are necessary for the performance of high-order cognitive and perceptual functions. Conversely, it is possible that certain pairs of cortical regions do not exchange information under normal brain function, and thus communication channels between them would not have evolved to be efficient [37]. Therefore, while our analyses indicate that the navigability of brain networks can be improved with explicit optimization, this improvement would potentially be at the cost of other important aspects of brain network organization.

Edge navigation centrality. We computed edge navigation centrality (ENC), weighted edge betweenness centrality (EBC) and binary EBC for the human connectome (group-averaged, $N = 360$ at 15% connection density, Fig. S13). All three edge centralities spanned several others of magnitude. ENC and weighted EBC were significantly but not strongly correlated (Pearson correlation coefficient $r = 0.03$), while a strong correlation was found between ENC and binary EBC ($r = 0.67$).

We found ENC to be more uniformly distributed across connections compared to both types of EBC (Fig. S13D). For instance, the top 15% most used connections were responsible for 59%, 76% and 83% of communication routes in navigation, binary shortest paths and weighted shortest paths, respectively (Fig. S13E). When ranking connections based on weight, we found the top 1% highest weighted connections to mediate 24% of weighted shortest paths; with the top 18% highest weighted connections responsible for 60% of weighted shortest paths (Fig. S13F). In contrast, the distribution of communication routes in binary shortest paths and navigation is, unsurprisingly, independent from connection weights.

The edge-based analysis of navigation centrality reiterates that navigation routing promotes a more resource-efficient distribution of the information traffic load than shortest paths, at the level of both nodes and connections.

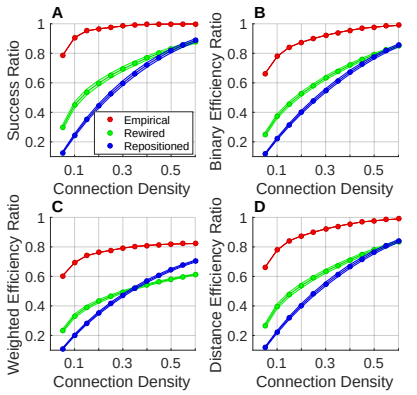

(a) $N = 256$

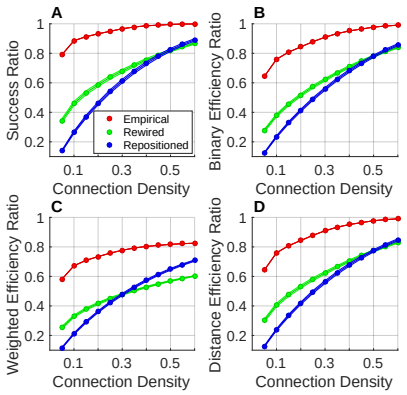

(b) $N = 512$

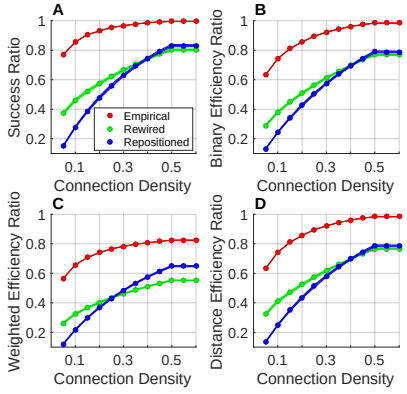

(c) $N = 1024$

Figure S1: Navigation performance of human connectomes with different parcellation resolutions. **(A-D)** Success ratio (S_R), binary efficiency ratio (E_R^{bin}), weighted efficiency ratio (E_R^{wei}) and distance efficiency ratio (E_R^{dis}) at different connection density thresholds. Empirical measures (red) for group-averaged connectomes were compared to 1000 ($N = 256$), 500 ($N = 512$) and 100 ($N = 1024$) rewired (green) and spatially repositioned (blue) null networks. Shading indicates 95% confidence intervals.

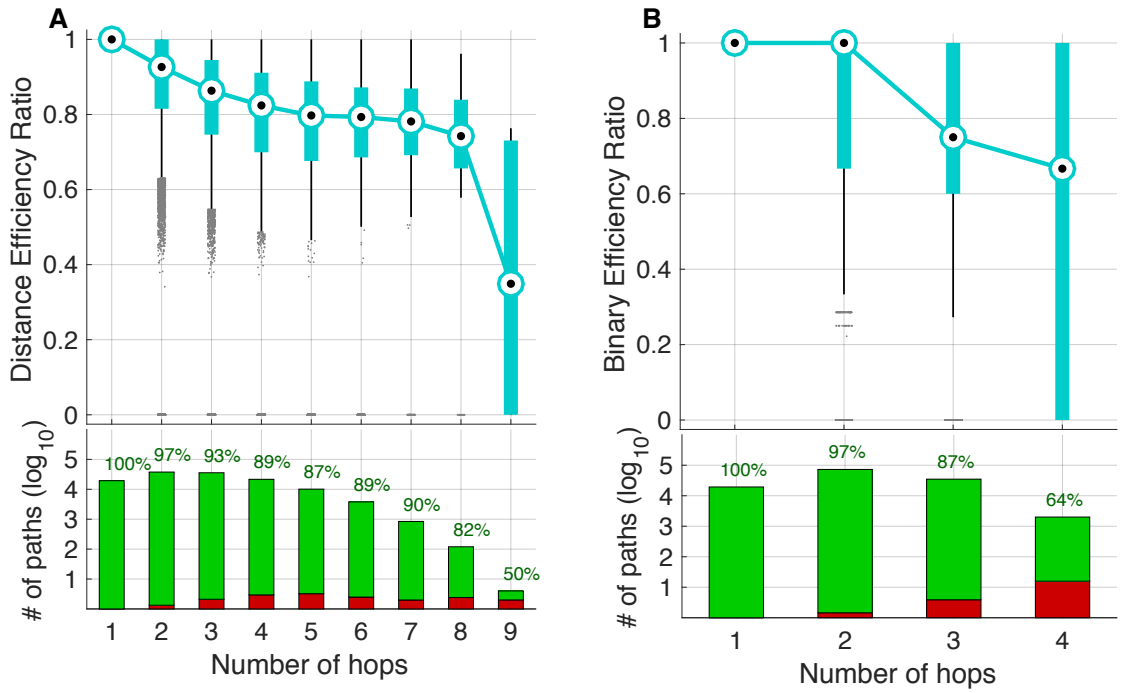

Figure S2: The performance of navigation routing in human SC stratified by shortest paths hop counts ($N = 360$ at 15% connection density). Blue boxplots indicate the quartiles of efficiency ratios of navigation paths benchmarked against shortest paths with matching hop count. Barplots show the number of shortest paths for a given hop count, with colors indicating the proportion of successful (green) and failed (red) navigation paths. Shortest paths computed over L^{dis} **(A)** and L^{bin} **(B)**.

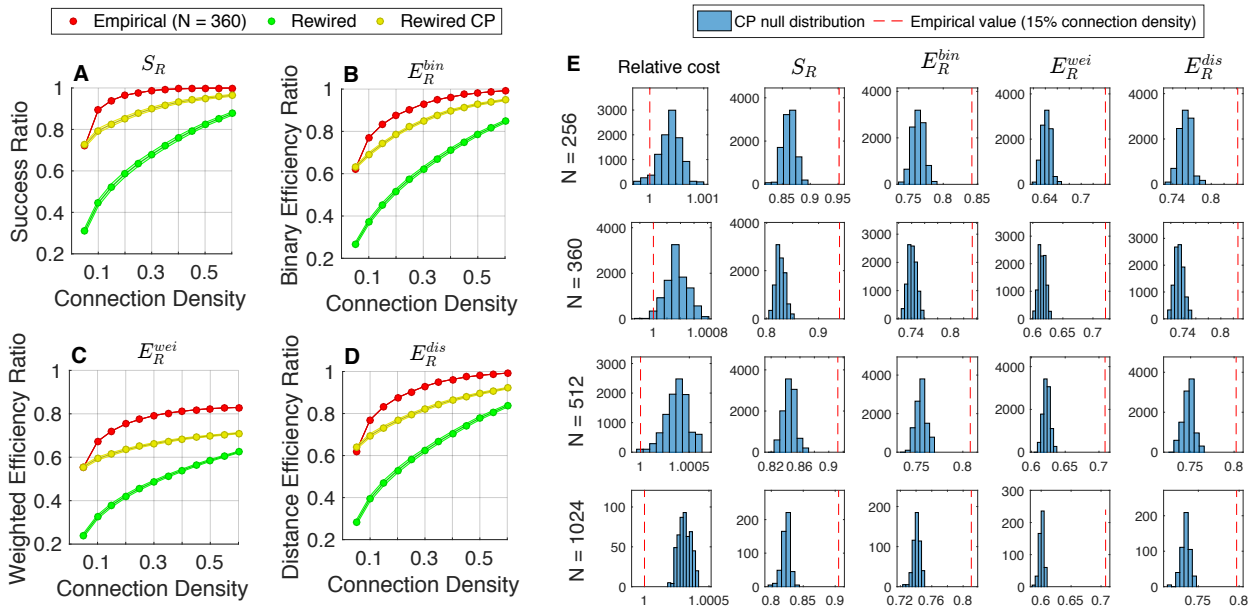

Figure S3: Navigation performance of the human connectome compared to cost-preserving null networks (group-averaged, $N = 360$, at 15% connection density). **(A-D)** Success ratio (S_R), binary efficiency ratio (E_R^{bin}), weighted efficiency ratio (E_R^{wei}) and distance efficiency ratio (E_R^{dis}) at several connection density thresholds. Curves show measures obtained for the human connectome (red), 10^4 rewired (green) and cost-preserving rewired (yellow) null networks. Shading indicates 95% confidence intervals. **(E)** Distributions of relative network cost ($cost_{null}/cost_{emp}$) and different navigation performance measures (columns) of ensembles of cost-preserving null networks, for several parcellation resolutions (rows). Cost-preserving ensembles consisted of 10^4 null networks for $N = 256, 360, 512$ and 500 null networks for $N = 1024$. Dashed red lines indicate empirical network cost and navigation performance measures. Cost-preserving null networks approximate connectome cost to an error margin of 0.1%. The human connectome remained significantly more navigable than cost-preserving rewired null networks across all parcellation resolutions and navigability measures.

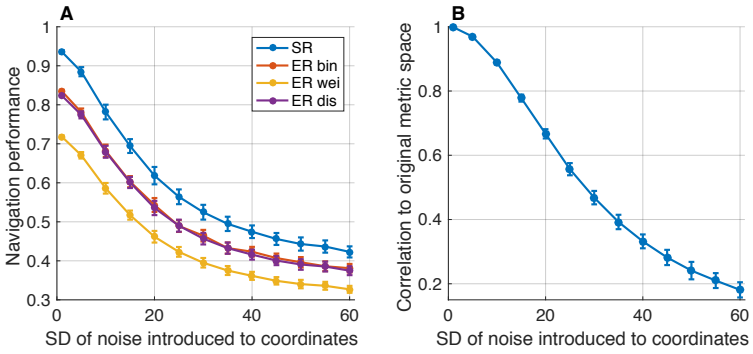

Figure S4: Navigation performance as a function of noise added to node centroid coordinates. Each node's three spatial coordinates were independently corrupted with additive Gaussian noise with zero mean and standard deviation (SD) that ranged between 0 and 60 (horizontal axis). **(A)** Navigation performance obtained by guiding navigation routing based on distances computed on the noisy coordinates. **(B)** Correlation between node distances computed on the original and noisy coordinates, as a function of standard deviation.

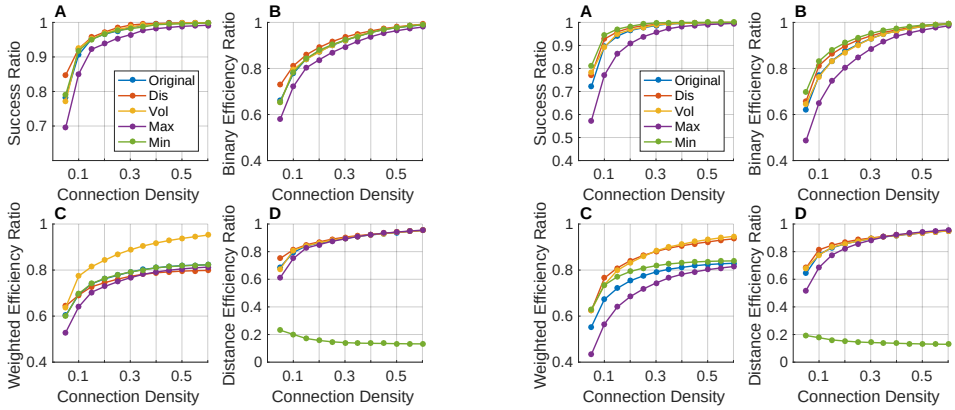

(a) $N = 256$ **(b)** $N = 360$

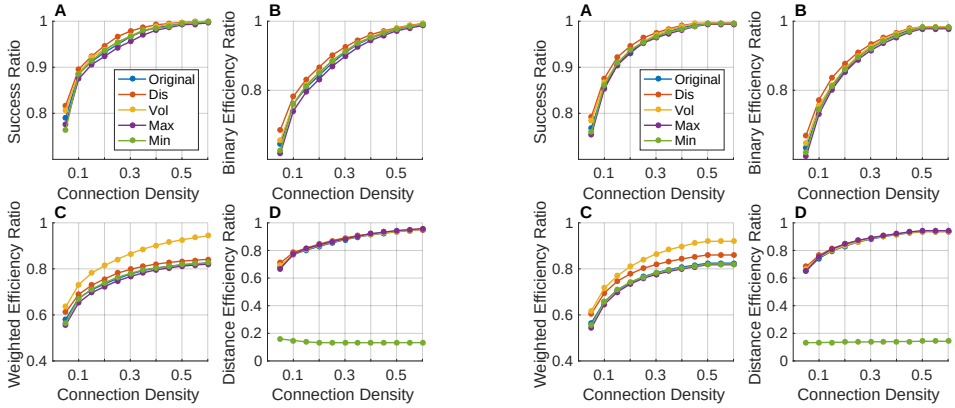

(c) $N = 512$ **(d)** $N = 1024$

Figure S5: Human connectome navigation performance computed for different distance measures and streamline count normalizations, for several parcellation resolutions (a-d). Results in the main text (blue curves) were computed using the Euclidean distance between node centroids and connectomes without normalization of streamline counts. **(A-D)** Curves show the Success ratio (S_R), binary efficiency ratio (E_R^{bin}), weighted efficiency ratio (E_R^{wei}) and distance efficiency ratio (E_R^{dis}) obtained from variations of the original configuration, for several connection density thresholds. The variations are: distance scaling of streamline counts ("Dis", orange curves); volume scaling of streamline counts ("Vol", yellow curves); maximum voxel distance as the distance measure between nodes ("Max", purple curves); and minimum voxel distance as the distance measure between nodes ("Min", green curves).

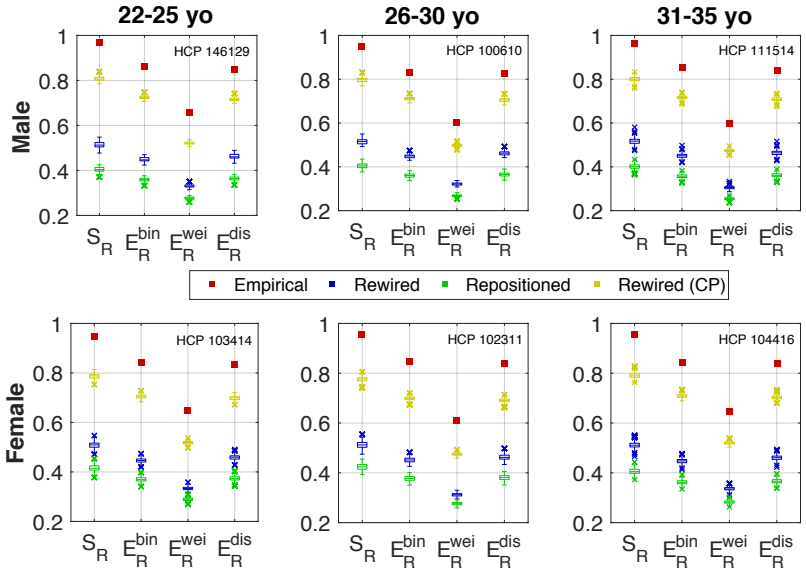

Figure S6: Connectome navigability of representative male and female individuals from each of the three age brackets investigated. Navigation performance was benchmarked against three null network models. Navigation performance was evaluated with respect to the success ratio (S_R), binary efficiency ratio (E_R^{bin}), weighted efficiency ratio (E_R^{wei}) and distance efficiency ratio (E_R^{dis}) (horizontal axis). The vertical axis shows the navigation performance of empirical (red), cost-preserving topologically randomized (yellow), topologically randomized (blue) and spatially randomized (green) null networks. Boxplots indicate the quartiles of performance measures obtained for null networks, with crosses denoting outliers.

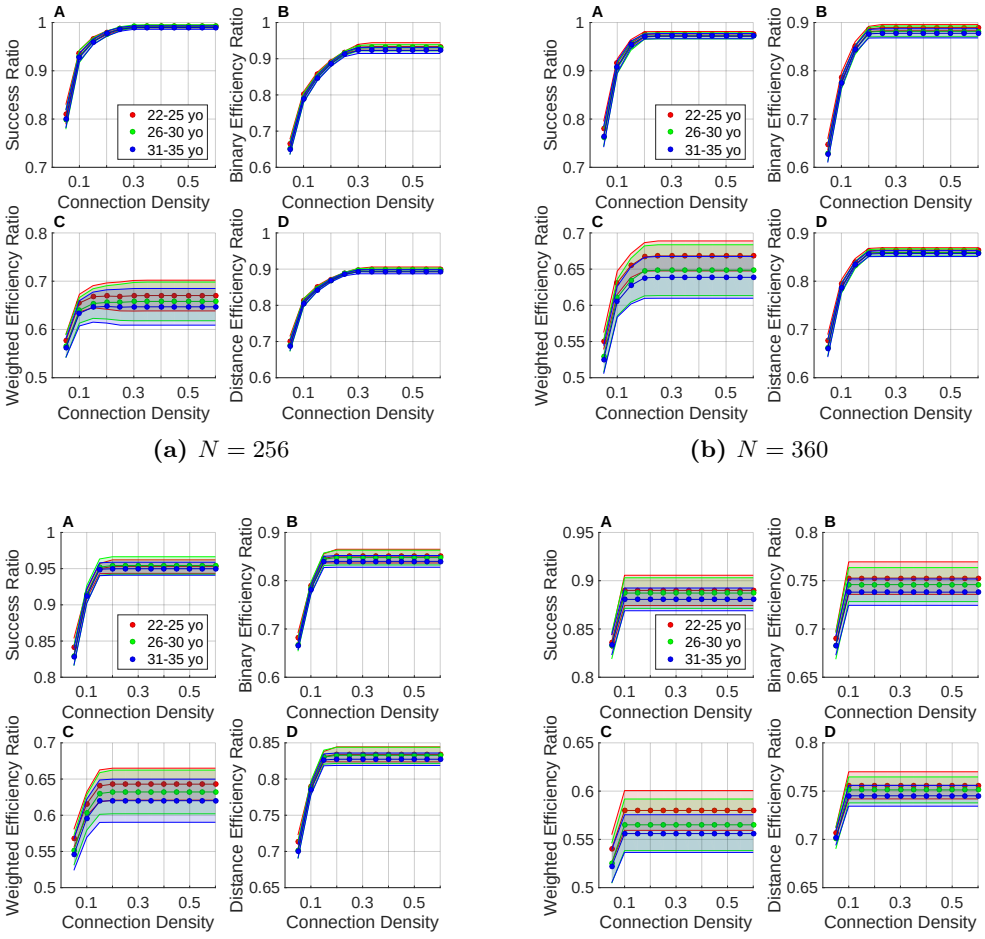

(a) $N = 256$ **(b)** $N = 360$

(c) $N = 512$ **(d)** $N = 1024$

Figure S7: Influence of age on connectome navigability for several parcellation resolutions (a-d). Navigation performance was evaluated for each individual and the average performance within each of three age brackets was computed as a function of connection density. **(A-D)** Success ratio (S_R), binary efficiency ratio (E_R^{bin}), weighted efficiency ratio (E_R^{wei}) and distance efficiency ratio (E_R^{dis}) averaged across individual age: 22–25 (red), 26–30 (green) and 31–35 (blue) years, at different connection density thresholds. Shading indicates 95% confidence intervals.

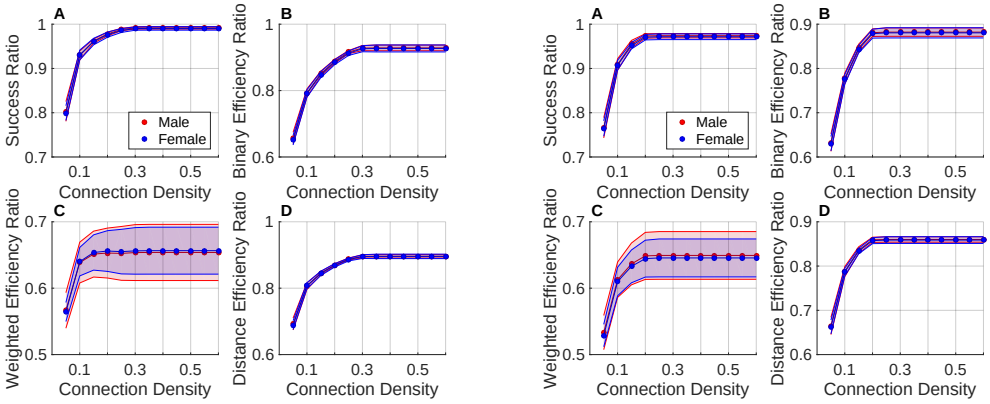

(a) $N = 256$ **(b)** $N = 360$

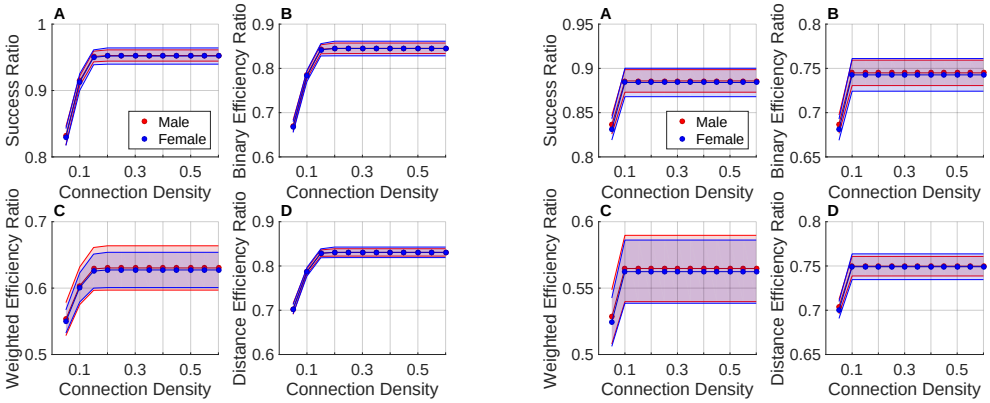

(c) $N = 512$ **(d)** $N = 1024$

Figure S8: Influence of sex on connectome navigability for several parcellation resolutions (a-d). Navigation performance was evaluated for each individual and the average of male and female navigability was assessed as a function of connection density. **(A-D)** Success ratio (S_R), binary efficiency ratio (E_R^{bin}), weighted efficiency ratio (E_R^{wei}) and distance efficiency ratio (E_R^{dis}) averaged across female (blue) and male (red) participants, at different connection density thresholds. Shading indicates 95% confidence intervals.

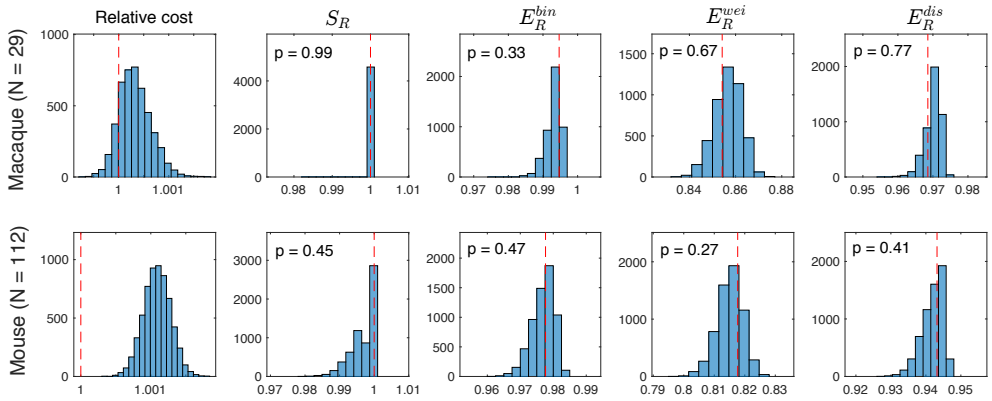

Figure S9: Navigation performance of non-human connectomes compared to cost-preserving rewired null networks. Distributions of relative network cost ($cost_{null}/cost_{emp}$) and different navigation performance measures (columns) of 5000 cost-preserving null networks, for the macaque (top row) and mouse (bottom row connectomes). Dashed red lines indicate empirical network cost and navigation performance measures. Cost-preserving null networks approximate connectome cost to an error margin of 0.1%. The null hypothesis of equality in navigation performance between the cost-preserving null networks and the empirical connectomes could not be rejected for the mouse and macaque (P >0.05).

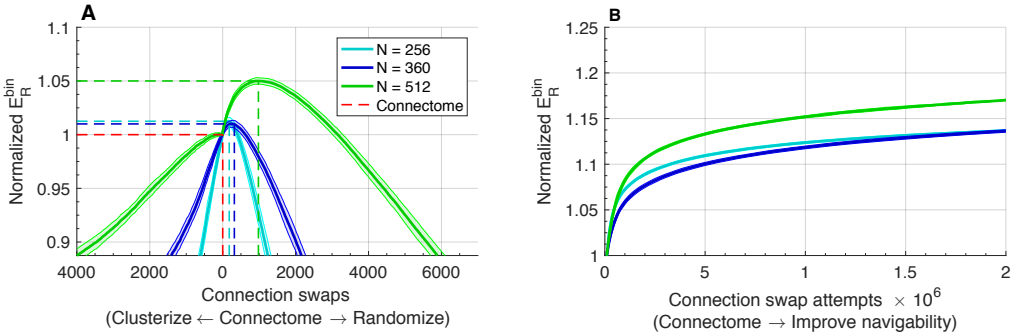

Figure S10: Navigation performance (E_R^{bin}) of progressively rewired connectome topologies (at 15% connection density). The E_R^{bin} of rewired topologies was normalized by the empirical value found for the human connectome. Curves indicate the mean values (inner line) and 95% confidence intervals (outer shadow) obtained from several runs of the rewiring routines. **(A)** Normalized E_R^{bin} of clusterized and randomized networks for 100 runs of the randomization-clusterizing procedure and different parcellation resolutions. Dashed lines show performance peaks (vertical axis) and number of connection swaps (horizontal axis), with red indicating the values obtained for the empirical brain. **(B)** Normalized E_R^{bin} obtained from direct optimization of the connectome's empirical E_R^{bin}, as a function of connection swap attempts, for 50 (N = 2560), 50 (N = 360) and 30 (N = 512) independent runs of the rewiring routine.

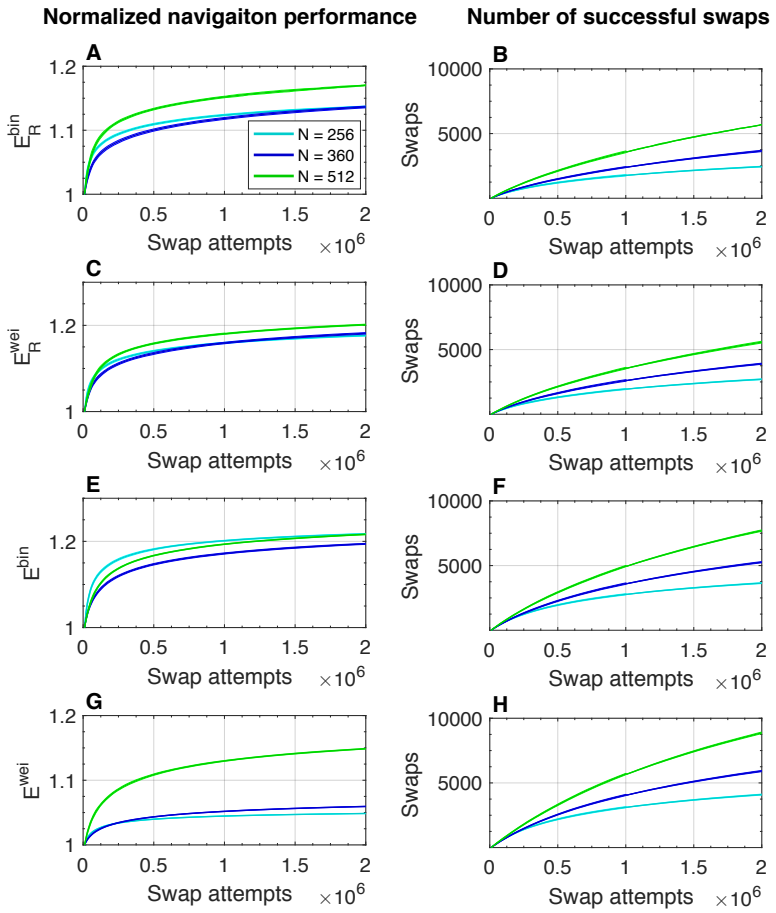

Figure S11: Optimization of the navigability of the human connectome (at 15% connection density) via progressive rewiring of empirical topology. Perturbations of connectome topology were carried out by random connection swaps that (i) preserved original network cost; (ii) resulted in an increase of given navigation performance measure; and (iii) preserved the original node degree distribution. Navigation measures obtained by topology rewiring were normalized by empirical values found for the human connectome. Curves indicate the mean values (inner line) and 95% confidence intervals (outer shadow) of 50 ($N = 256$, light blue), 50 ($N = 360$, dark blue) and 30 ($N = 512$, green) independent optimization runs. **(A,C,E,G)** Normalized navigation performances for 2×10^6 connection swap attempts. **(B,D,F,H)** Number of successful connection swaps as a function of the number of swap attempts. Successful swaps simultaneously satisfied conditions (i), (ii) and (iii).

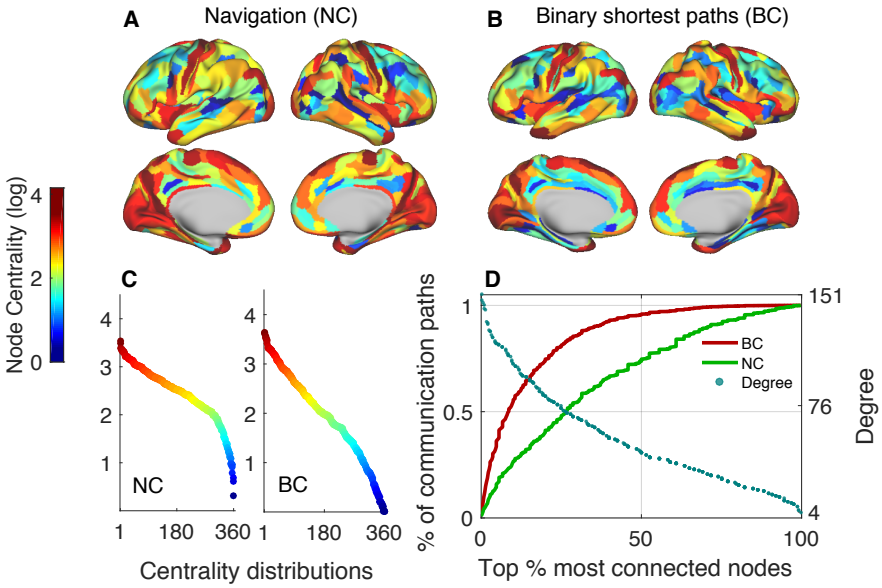

Figure S12: Comparison between navigation (NC) and binary betweenness (BC) node centralities for $N = 360$ at 15% connection density. Centrality values are logarithmically scaled. NC **(A)** and BC **(B)** projected onto the cortical surface. **(C)** NC (right) and BC (left) sorted from highest to lowest values **(D)** Relationship between the cumulative sum of centrality measures and degree. The horizontal axis is a percentage ranking of nodes from highest to lowest degree (e.g., for $N = 360$, the 10% most connected nodes are the 36 nodes with highest degree). Solid curves (left-hand vertical axis) represent the cumulative sum of BC (red) and NC (green) over all nodes ordered from most to least connected, divided by the total number of communication paths in the network, indicating the fraction of communication paths mediated by nodes. Blue dots (right-hand vertical axis) show the original degree associated with each percentage of most connected nodes.

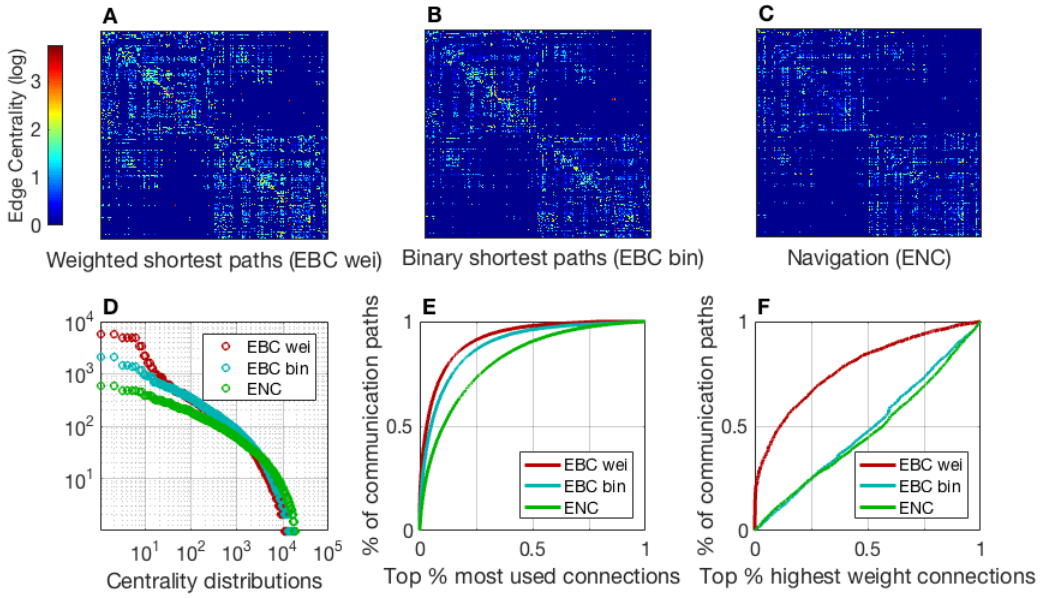

Figure S13: Comparison between edge navigation centrality (ENC), weighted edge betweenness centrality (EBC) and binary EBC (group-averaged connectome, $N = 360$, at 15% connection density). **(A-C)** Matrix representation of logarithmically scaled edge centrality values. **(D)** Edge centrality distributions for navigation (green), binary shortest paths (blue) and weighted shortest paths (red), sorted from highest to lowest values. **(E)** Fraction of communication paths mediated by connections. Connections were sorted according to their centrality values. The vertical axis shows the cumulative sum of centrality measures divided by the total number of communication paths in the network. **(F)** Fraction of communication paths mediated by connections, with connections sorted by weight. The vertical axis shows the cumulative sum of centrality measures divided by the total number of communication paths in the network.

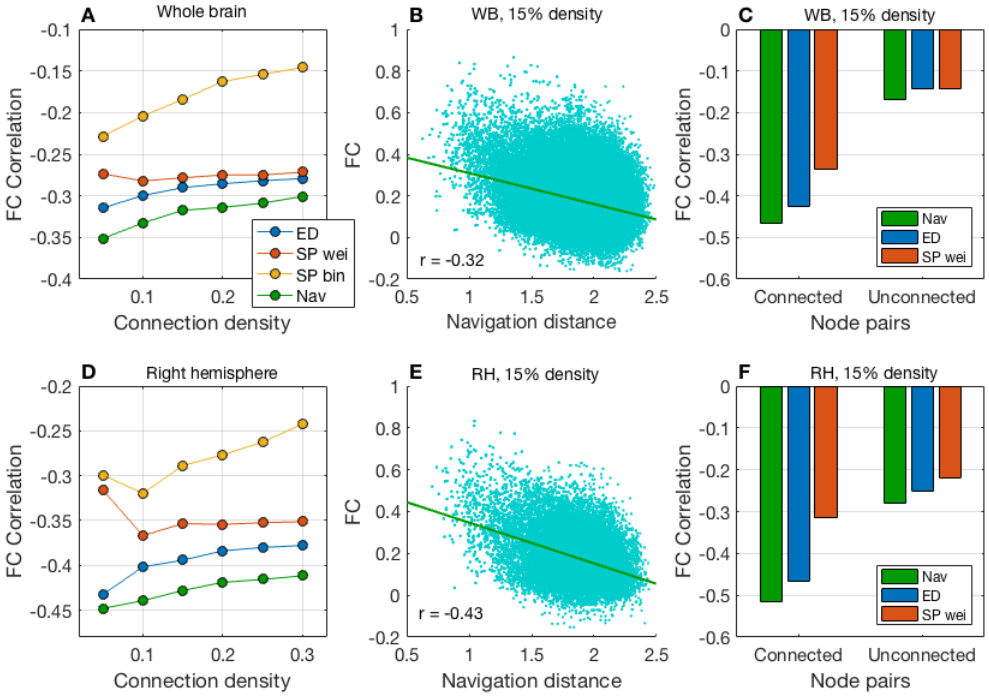

Figure S14: Correlation between FC and network communication measures (group-averaged connectome, $N = 360$, at 15% connection density). Correlations were computed for successful navigation paths. The navigation distance of nodes i, j was defined as the log of the sum of connection distances along the navigation path from i to j. **(A)** Whole brain correlations between FC and Euclidean distance (blue), weighted shortest paths (orange), binary shortest paths (yellow) and navigation distance (green). **(B)** Scatter plot between navigation distances and FC for all brain regions. Green line indicate the linear fit between the two measures. **(C)** FC correlations stratified for structurally connected and unconnected node pairs. **(D-F)** Right hemisphere equivalent of panels A-C.

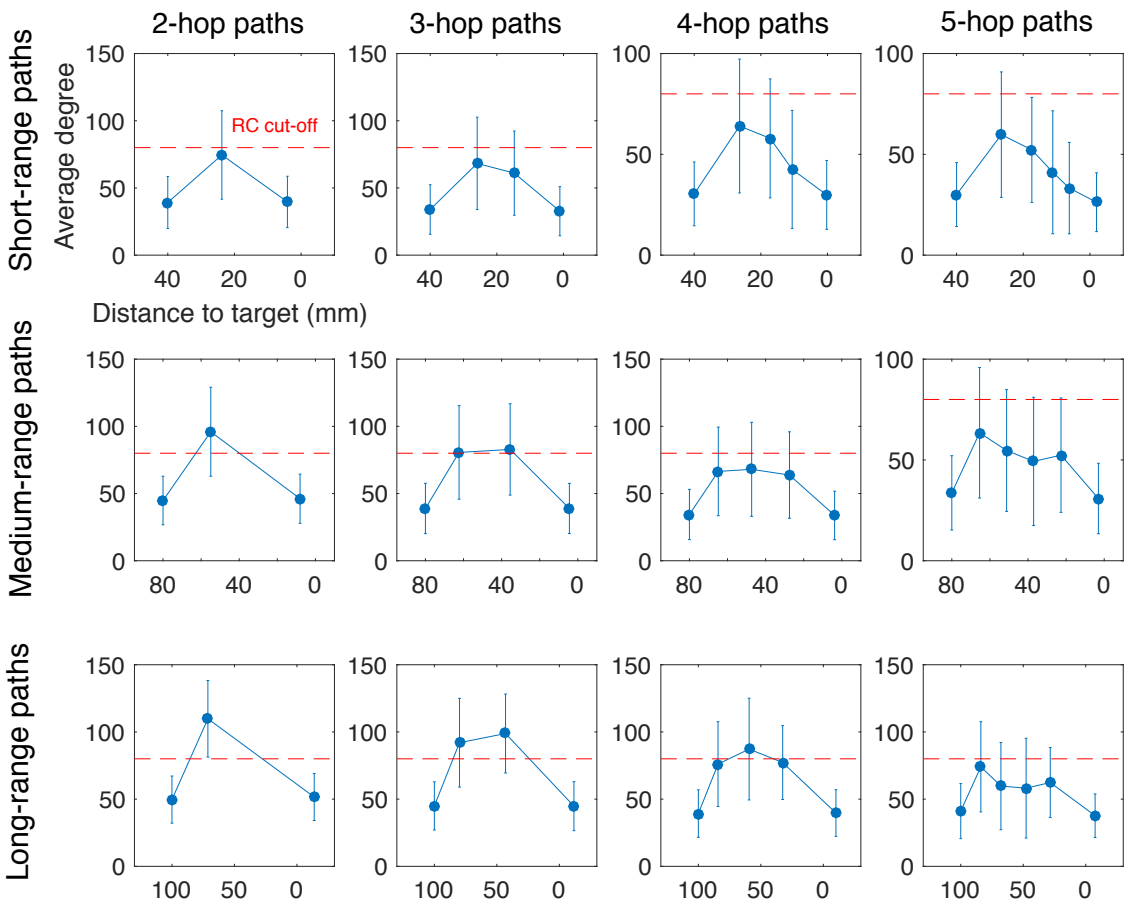

Figure S15: Structure of navigation paths between non rich club nodes ($N = 360$ at 15% connection density). Top, middle and bottom rows depict, respectively, short- (Euclidean distance from source to target nodes d_{st} $\leqslant$50 mm), medium- (50 mm$< d_{st} \leqslant$100 mm) and long-range paths (d_{st} >100 mm). Columns show paths 2 to 5 hops long. For each panel, the horizontal axis shows the average distance to the target, while the vertical axis shows the average degree (and standard deviation) of nodes along the path. The red dashed line marks the cut-off degree $k = 80$ for the binary rich club (computed as in [38]). Navigation paths follow a "zoom-out/zoom-in" structure, proceeding allowing sequences of low-, high- and low-degree nodes. This path structure is facilitated by a heterogeneous degree distribution and high clustering coefficient. First, information travels via peripheral connections around the locally clustered vicinity of the source. Once it reaches a high-degree node, it is forwarded towards the target via long-range connections, quickly traversing large distances in a small number of hops. Finally, once at the destination's vicinity, the information again makes use of local clustering to home in on the target. This mechanism for information transfer is in line with the notion of the brain as a small world network that balances integration—high-degree nodes forming long-range connections that provide quick access to different parts of the brain—and segregation—specialized, locally clustered, information processing modules responsible for specific tasks. The rich club of highly interconnected hubs is predominantly used for long-range paths, while short- and medium-range communication takes place mostly via peripheral routes.

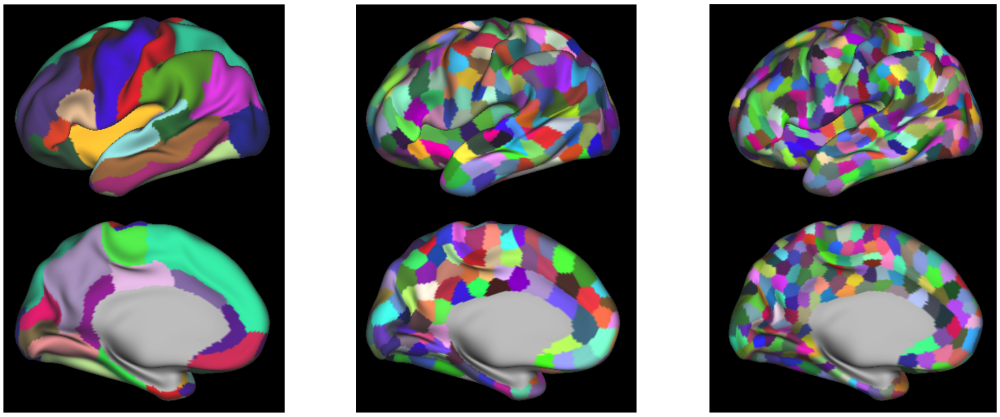

(a) $N = 68$ **(b)** $N = 512$ **(c)** $N = 1024$

Figure S16: Cortical surface parcellation (left hemisphere). **(A)** Input low-resolution parcellation delineating 68 cortical regions. Output high-resolution parcellations with 512 **(B)** and 1024 **(C)** regions. All output sub-regions are contiguous, tile-shaped and have approximately the same surface area, while respecting the anatomical boundaries defined by the original 68 region atlas.

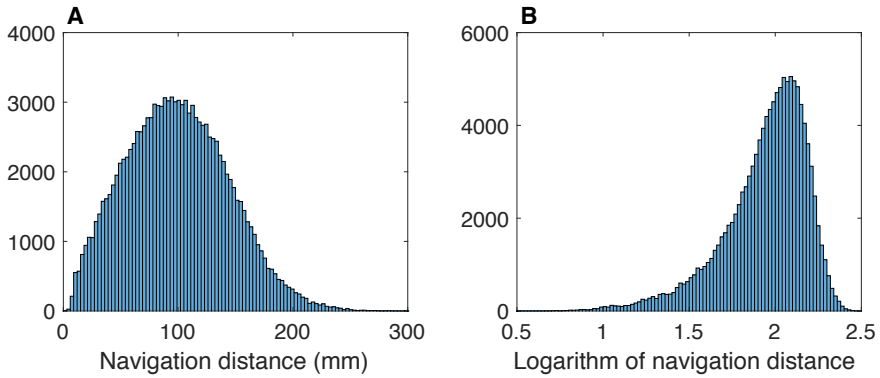

Figure S17: Distribution of raw **(A)** and log-transformed **(B)** navigation path lengths between all pairs of nodes ($N = 360$ at 15% connection density threshold).

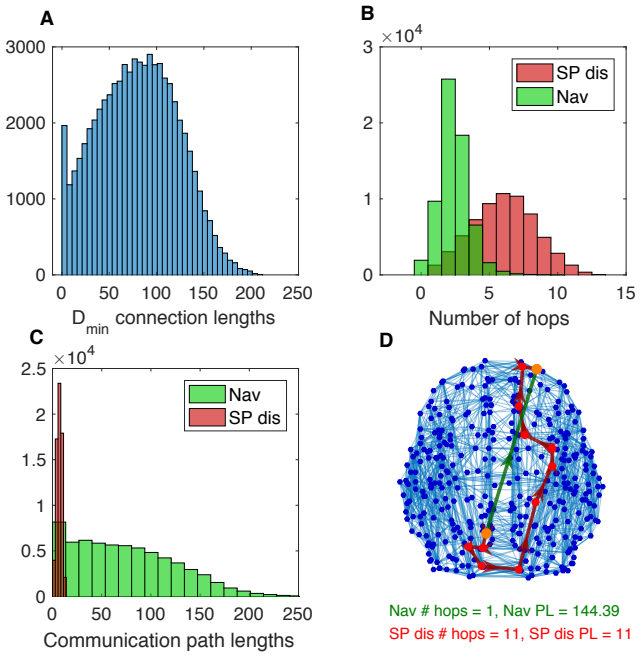

Figure S18: Exploration of navigation and distance-based shortest paths using minimum voxel distance (group-averaged connectome, $N = 360$ at 15% connection density). **(A)** Distribution of minium voxel distances between node pairs. **(B)** Distribution of hop counts in navigation and distance-based shortest paths. **(C)** Distribution of path lengths in navigation and distance-based shortest paths. **(D)** Example of a distance-based shortest path and navigation path between structurally connected nodes.

References

[1] S. W. Oh, J. A. Harris, L. Ng, B. Winslow, N. Cain, S. Mihalas, Q. Wang, C. Lau, L. Kuan, A. M. Henry, M. T. Mortrud, B. Ouellette, T. N. Nguyen, S. A. Sorensen, C. R. Slaughterbeck, W. Wakeman, Y. Li, D. Feng, A. Ho, E. Nicholas, K. E. Hirokawa, P. Bohn, K. M. Joines, H. Peng, M. J. Hawrylycz, J. W. Phillips, J. G. Hohmann, P. Wohnoutka, C. R. Gerfen, C. Koch, A. Bernard, C. Dang, A. R. Jones, and H. Zeng, "A mesoscale connectome of the mouse brain," *Nature*, vol. 508, pp. 207–14, Apr 2014.

[2] M. Rubinov, R. J. F. Ypma, C. Watson, and E. T. Bullmore, "Wiring cost and topological participation of the mouse brain connectome," *Proc Natl Acad Sci U S A*, vol. 112, pp. 10032–7, Aug 2015.

[3] N. T. Markov, M. Ercsey-Ravasz, C. Lamy, A. R. Ribeiro Gomes, L. Magrou, P. Misery, P. Giroud, P. Barone, C. Dehay, Z. Toroczkai, K. Knoblauch, D. C. Van Essen, and H. Kennedy, "The role of long-range connections on the specificity of the macaque interareal cortical network," *Proc Natl Acad Sci U S A*, vol. 110, pp. 5187–92, Mar 2013.

[4] N. T. Markov, M. M. Ercsey-Ravasz, A. R. Ribeiro Gomes, C. Lamy, L. Magrou, J. Vezoli, P. Misery, A. Falchier, R. Quilodran, M. A. Gariel, J. Sallet, R. Gamanut, C. Huissoud, S. Clavagnier, P. Giroud, D. Sappey-Marinier, P. Barone, C. Dehay, Z. Toroczkai, K. Knoblauch, D. C. Van Essen, and H. Kennedy, "A weighted and directed interareal connectivity matrix for macaque cerebral cortex," *Cereb Cortex*, vol. 24, pp. 17–36, Jan 2014.

[5] D. C. Van Essen, S. M. Smith, D. M. Barch, T. E. J. Behrens, E. Yacoub, K. Ugurbil, and WU-Minn HCP Consortium, "The wu-minn human connectome project: an overview," *Neuroimage*, vol. 80, pp. 62–79, Oct 2013.

[6] M. F. Glasser, S. N. Sotiropoulos, J. A. Wilson, T. S. Coalson, B. Fischl, J. L. Andersson, J. Xu, S. Jbabdi, M. Webster, J. R. Polimeni, D. C. Van Essen, M. Jenkinson, and WU-Minn HCP Consortium, "The minimal preprocessing pipelines for the human connectome project," *Neuroimage*, vol. 80, pp. 105–24, Oct 2013.

[7] S. N. Sotiropoulos, S. Jbabdi, J. Xu, J. L. Andersson, S. Moeller, E. J. Auerbach, M. F. Glasser, M. Hernandez, G. Sapiro, M. Jenkinson, D. A. Feinberg, E. Yacoub, C. Lenglet, D. C. Van Essen, K. Ugurbil, T. E. J. Behrens, and WU-Minn HCP Consortium, "Advances in diffusion mri acquisition and processing in the human connectome project," *Neuroimage*, vol. 80, pp. 125–43, Oct 2013.

[8] S. M. Smith, C. F. Beckmann, J. Andersson, E. J. Auerbach, J. Bijsterbosch, G. Douaud, E. Duff, D. A. Feinberg, L. Griffanti, M. P. Harms, M. Kelly, T. Laumann, K. L. Miller, S. Moeller, S. Petersen, J. Power, G. Salimi-Khorshidi, A. Z. Snyder, A. T. Vu, M. W. Woolrich, J. Xu, E. Yacoub, K. Uğurbil, D. C. Van Essen, M. F. Glasser, and WU-Minn HCP Consortium, "Resting-state fmri in the human connectome project," *Neuroimage*, vol. 80, pp. 144–68, Oct 2013.

[9] A. Zalesky, A. Fornito, I. H. Harding, L. Cocchi, M. Yücel, C. Pantelis, and E. T. Bullmore, "Whole-brain anatomical networks: does the choice of nodes matter?," *Neuroimage*, vol. 50, pp. 970–83, Apr 2010.

[10] M. F. Glasser, T. S. Coalson, E. C. Robinson, C. D. Hacker, J. Harwell, E. Yacoub, K. Ugurbil, J. Andersson, C. F. Beckmann, M. Jenkinson, S. M. Smith, and D. C. Van Essen, "A multi-modal parcellation of human cerebral cortex," *Nature*, vol. 536, pp. 171–178, 08 2016.

[11] R. S. Desikan, F. Ségonne, B. Fischl, B. T. Quinn, B. C. Dickerson, D. Blacker, R. L. Buckner, A. M. Dale, R. P. Maguire, B. T. Hyman, M. S. Albert, and R. J. Killiany, "An automated labeling system for subdividing the human cerebral cortex on mri scans into gyral based regions of interest," *Neuroimage*, vol. 31, pp. 968–80, Jul 2006.

[12] D. Arthur and S. Vassilvitskii, "K-means++: The advantages of careful seeding," in *Proceedings of the eighteenth annual ACM-SIAM symposium on Discrete algorithms*, pp. 1027–1035, Society for Industrial and Applied Mathematics, 2007.

[13] D. S. Marcus, J. Harwell, T. Olsen, M. Hodge, M. F. Glasser, F. Prior, M. Jenkinson, T. Laumann, S. W. Curtiss, and D. C. Van Essen, "Informatics and data mining tools and strategies for the human connectome project," *Front Neuroinform*, vol. 5, p. 4, 2011.

[14] K. H. Maier-Hein, P. F. Neher, J.-C. Houde, M.-A. Côté, E. Garyfallidis, J. Zhong, M. Chamberland, F.-C. Yeh, Y.-C. Lin, Q. Ji, W. E. Reddick, J. O. Glass, D. Q. Chen, Y. Feng, C. Gao, Y. Wu, J. Ma, H. Renjie, Q. Li, C.-F. Westin, S. Deslauriers-Gauthier, J. O. O. González, M. Paquette, S. St-Jean, G. Girard, F. Rheault, J. Sidhu, C. M. W. Tax, F. Guo, H. Y. Mesri, S. Dávid, M. Froeling, A. M. Heemskerk, A. Leemans, A. Boré, B. Pinsard, C. Bedetti, M. Desrosiers, S. Brambati, J. Doyon, A. Sarica, R. Vasta, A. Cerasa, A. Quattrone, J. Yeatman, A. R. Khan, W. Hodges, S. Alexander, D. Romascano, M. Barakovic, A. Auría, O. Esteban, A. Lemkaddem, J.-P. Thiran, H. E. Cetingul, B. L. Odry, B. Mailhe, M. S. Nadar, F. Pizzagalli, G. Prasad, J. E. Villalon-Reina, J. Galvis, P. M. Thompson, F. D. S. Requejo, P. L. Laguna, L. M. Lacerda, R. Barrett, F. Dell'Acqua, M. Catani, L. Petit, E. Caruyer, A. Daducci, T. B. Dyrby, T. Holland-Letz, C. C. Hilgetag, B. Stieltjes, and M. Descoteaux, "The challenge of mapping the human connectome based on diffusion tractography," *Nat Commun*, vol. 8, p. 1349, Nov 2017.

[15] J.-D. Tournier, F. Calamante, and A. Connelly, "Mrtrix: Diffusion tractography in crossing fiber regions," *International Journal of Imaging Systems and Technology*, vol. 22, 03 2012.

[16] J. Goñi, M. P. van den Heuvel, A. Avena-Koenigsberger, N. Velez de Mendizabal, R. F. Betzel, A. Griffa, P. Hagmann, B. Corominas-Murtra, J.-P. Thiran, and O. Sporns, "Resting-brain functional connectivity predicted by analytic measures of network communication," *Proc Natl Acad Sci U S A*, vol. 111, pp. 833–8, Jan 2014.

[17] A. Avena-Koenigsberger, B. Mišić, R. X. Hawkins, A. Griffa, P. Hagmann, J. Goñi, and O. Sporns, "Path ensembles and a tradeoff between communication efficiency and resilience in the human connectome," *Brain Structure and Function*, pp. 1–16, 2016.

[18] A. Fornito, A. Zalesky, and M. Breakspear, "Graph analysis of the human connectome: promise, progress, and pitfalls," *Neuroimage*, vol. 80, pp. 426–44, Oct 2013.

[19] A. Fornito, A. Zalesky, and E. T. Bullmore, *Fundamentals of brain network analysis*. 2016.

[20] M. Rubinov and O. Sporns, "Complex network measures of brain connectivity: uses and interpretations," *Neuroimage*, vol. 52, pp. 1059–69, Sep 2010.

[21] S. Maslov and K. Sneppen, "Specificity and stability in topology of protein networks," *Science*, vol. 296, pp. 910–3, May 2002.

[22] R. F. Betzel, L. Byrge, Y. He, J. Goñi, X.-N. Zuo, and O. Sporns, "Changes in structural and functional connectivity among resting-state networks across the human lifespan," *Neuroimage*, vol. 102 Pt 2, pp. 345–57, Nov 2014.

[23] P. Hagmann, L. Cammoun, X. Gigandet, R. Meuli, C. J. Honey, V. J. Wedeen, and O. Sporns, "Mapping the structural core of human cerebral cortex," *PLoS Biol*, vol. 6, p. e159, Jul 2008.

[24] A. Zalesky and A. Fornito, "A dti-derived measure of cortico-cortical connectivity," *IEEE Trans Med Imaging*, vol. 28, pp. 1023–36, Jul 2009.

[25] P. E. Vértes, A. F. Alexander-Bloch, N. Gogtay, J. N. Giedd, J. L. Rapoport, and E. T. Bullmore, "Simple models of human brain functional networks," *Proc Natl Acad Sci U S A*, vol. 109, pp. 5868–73, Apr 2012.

[26] A. F. Alexander-Bloch, P. E. Vértes, R. Stidd, F. Lalonde, L. Clasen, J. Rapoport, J. Giedd, E. T. Bullmore, and N. Gogtay, "The anatomical distance of functional connections predicts brain network topology in health and schizophrenia," *Cereb Cortex*, vol. 23, pp. 127–38, Jan 2013.

[27] R. F. Betzel, A. Avena-Koenigsberger, J. Goñi, Y. He, M. A. de Reus, A. Griffa, P. E. Vértes, B. Mišic, J.-P. Thiran, P. Hagmann, M. van den Heuvel, X.-N. Zuo, E. T. Bullmore, and O. Sporns, "Generative models of the human connectome," *Neuroimage*, vol. 124, pp. 1054–64, Jan 2016.

[28] J. A. Roberts, A. Perry, A. R. Lord, G. Roberts, P. B. Mitchell, R. E. Smith, F. Calamante, and M. Breakspear, "The contribution of geometry to the human connectome," *Neuroimage*, vol. 124, pp. 379–93, Jan 2016.

[29] E. Bullmore and O. Sporns, "The economy of brain network organization," *Nat Rev Neurosci*, vol. 13, pp. 336–49, Apr 2012.

[30] M. Kaiser, R. Martin, P. Andras, and M. P. Young, "Simulation of robustness against lesions of cortical networks," *Eur J Neurosci*, vol. 25, pp. 3185–92, May 2007.

[31] R. F. Betzel and D. S. Bassett, "The specificity and robustness of long-distance connections in weighted, interareal connectomes," *arXiv preprint arXiv:1711.03809*, 2017.

[32] K. Zilles, N. Palomero-Gallagher, and K. Amunts, "Development of cortical folding during evolution and ontogeny," *Trends Neurosci*, vol. 36, pp. 275–84, May 2013.

[33] M. D. Gregory, J. S. Kippenhan, D. Dickinson, J. Carrasco, V. S. Mattay, D. R. Weinberger, and K. F. Berman, "Regional variations in brain gyrification are associated with general cognitive ability in humans," *Curr Biol*, vol. 26, pp. 1301–5, 05 2016.

[34] M. Kaiser and C. C. Hilgetag, "Nonoptimal component placement, but short processing paths, due to long-distance projections in neural systems," *PLoS Comput Biol*, vol. 2, p. e95, Jul 2006.

[35] Albert, Jeong, and Barabasi, "Error and attack tolerance of complex networks," *Nature*, vol. 406, pp. 378–82, Jul 2000.

[36] A. Fornito, A. Zalesky, and M. Breakspear, "The connectomics of brain disorders," *Nat Rev Neurosci*, vol. 16, pp. 159–72, Mar 2015.

[37] A. Avena-Koenigsberger, B. Misic, and O. Sporns, "Communication dynamics in complex brain networks," *Nat Rev Neurosci*, vol. 19, pp. 17–33, Dec 2017.

[38] M. P. van den Heuvel, R. S. Kahn, J. Goñi, and O. Sporns, "High-cost, high-capacity backbone for global brain communication," *Proc Natl Acad Sci U S A*, vol. 109, pp. 11372–7, Jul 2012.